

This discussion paper is/has been under review for the journal The Cryosphere (TC).
Please refer to the corresponding final paper in TC if available.

Satellite-Derived Volume Loss Rates and Glacier Speeds for the Cordillera Darwin Icefield, Chile

A. K. Melkonian¹, M. J. Willis¹, M. E. Pritchard¹, A. Rivera^{2,3}, F. Bown², and S. A. Bernstein⁴

¹Department of Earth and Atmospheric Sciences, Cornell University, Ithaca, New York, USA

²Centro de Estudios Científicos (CECs), Valdivia, Chile

³Departamento de Geografía, Universidad de Chile, Santiago, Chile

⁴St. Timothy's School, 8400 Greenspring Ave, Stevenson, MD, 21153, USA

Received: 12 July 2012 – Accepted: 31 July 2012 – Published: 31 August 2012

Correspondence to: A. K. Melkonian (akm26@cornell.edu)

Published by Copernicus Publications on behalf of the European Geosciences Union.

3503

Abstract

We produce the first icefield-wide volume change rate and glacier velocity estimates for the Cordillera Darwin Icefield (CDI), a 2605 km² temperate icefield in Southern Chile (69.6° W, 54.6° S). Velocities are measured from optical and radar imagery between 2001–2011. Thirty-seven digital elevation models (DEMs) from ASTER and the SRTM are stacked and a weighted linear regression is applied to elevations on a pixel-by-pixel basis to estimate volume change rates.

The CDI lost mass at an average rate of $3.9 \pm 0.3 \text{ Gt yr}^{-1}$ between 2000 and 2011, equivalent to a sea level rise (SLR) of $0.01 \pm 0.001 \text{ mm yr}^{-1}$. Thinning is widespread, with concentrations near the front of two northern glaciers (Marinelli, Darwin) and one western (CDI-08) glacier. Thickening is apparent in the south, most notably over the advancing Garibaldi Glacier. We attribute this thinning pattern to warmer temperatures, particularly in the north, which triggered rapid retreat at Marinelli Glacier ($\sim 4 \text{ km}$ from 2001–2011).

Velocities are obtained over many of the swiftly flowing glaciers for the first time. We provide a repeat speed timeseries at the Marinelli Glacier. Maximum front speeds there accelerated from 7.5 m day^{-1} in 2001 to 9.5 m day^{-1} in 2003, to a peak of 10 m day^{-1} in 2011.

1 Introduction

The Cordillera Darwin Icefield (CDI) is a small icefield, located in the southernmost Andes (Fig. 1) in Tierra del Fuego. The temperate icefield is coalesced around two main mountain peaks, Mount Darwin 2469 m a.s.l., (e.g., Koppes et al., 2009) and Mount Sarmiento 2300 m a.s.l., (e.g., Strelin et al., 2008) and covers 2605 km², measured from ice outlines derived from satellite imagery acquired from 2001 to 2004. It extends roughly 200 km west-to-east from 71.8° W to 68.5° W and roughly 50 km south-to-north from 54.9° S to 54.2° S. The icefield is bounded to the north by the Almirantazgo Ford

3504

and the Beagle Channel in the south. Precipitation during the winter comes predominantly from the south/southwest (Holmlund and Fuenzalida, 1995), and the E–W orientation of the CDI leads to an orographic effect with greater snowfall on southern glaciers and drier, warmer conditions on northern glaciers (Holmlund and Fuenzalida, 1995; Strelin and Iturraspe, 2007; Koppes et al., 2009).

There are few studies on the CDI compared to other temperate icefields (Masiokas et al., 2009; Lopez et al., 2010), such as the Alaskan icefields, the Northern Patagonian Icefield (NPI) and the Southern Patagonian Icefield (SPI) (e.g., Arendt et al., 2002; Rignot et al., 2003; Berthier et al., 2007, 2010; Glasser et al., 2011; Willis et al., 2012a). Climate and mass balance studies are scarce for southern hemisphere ice bodies outside of Antarctica (Holmlund and Fuenzalida, 1995; Lopez et al., 2010), due to the difficult access and weather. Here we focus on the third largest temperate icefield in the southern hemisphere (Bown et al., 2013), which along with the NPI and SPI, has experienced a rapid reduction in ice-covered area (Rivera et al., 2007; Masiokas et al., 2009; Lopez et al., 2010; Willis et al., 2012b).

The loss of ice at the CDI has been attributed to climatic changes in the region, including warming during the 20th century (Holmlund and Fuenzalida, 1995; Lopez et al., 2010) (from climate station data) in conjunction with decreased precipitation (Quintana, 2004). Since the mid-20th century, and despite a reduction in regional precipitation, the CDI in particular has experienced increased precipitation on its southern side (Strelin and Iturraspe, 2007), with decreased precipitation and warmer temperatures on its northern side inferred from NCEP-NCAR climate model results (Koppes et al., 2009).

Temperate icefields are disproportionately large contributors to SLR (e.g., Arendt et al., 2002; Rignot et al., 2003); Rignot et al., 2003 claim this is particularly true of the Patagonian glaciers, which they say account for 9% of the non-polar contribution to SLR. The CDI, along with the NPI and SPI, provides an opportunity to examine the response of different glaciers (e.g. calving vs. non-calving) in different climates (maritime on the southern side versus more continental on the northern side) to regional changes in climate (Holmlund and Fuenzalida, 1995), and unlike the NPI and SPI the

3505

contribution of the CDI to SLR has not yet been estimated (Lopez et al., 2010). Finally, the CDI is the closest icefield to the Antarctic Peninsula, a region that has also experienced significant warming. Thinning and acceleration have been observed on glaciers in the Antarctic Peninsula and the NPI (Pritchard and Vaughan, 2007; Willis et al., 2012a), we assess whether this is the case for any glaciers on the CDI. Mass loss at the CDI might be contaminating GRACE measurements of nearby icefields (e.g. the NPI, SPI and Antarctic Peninsula), so our constraints on the mass loss rate occurring at the CDI will help isolate this signal.

In this study we calculate both the elevation change rates ($\frac{dh}{dt}$) over the entire CDI and measure glacier velocities using pixel-tracking applied to pairs of optical and radar images. With $\frac{dh}{dt}$ and an assumed ice density we can estimate the mass change rate and give a measurement of the CDI's contribution to SLR, allowing us to compare its SLR contribution to other icefields. We can also use the surface elevation change rates to identify which glaciers are providing the largest contribution to SLR and should be the focus of further study. Additionally, measuring glacier velocities allows an estimate of mass flux out of the glacier if the thickness is known. Our results will provide a baseline measurement over many glaciers and areas of the icefield for which ice velocities have not been measured.

2 Methods

2.1 Data preparation

The Advanced Spaceborne Thermal Emission and Reflection Radiometer (ASTER) has a stereo-imaging capability, enabling DEMs to be generated on-demand by NASA's Land Processes Distributed Active Archive Center (LP DAAC) (Fujisada et al., 2005). ASTER DEMs (product 14) are used to calculate $\frac{dh}{dt}$, while band 3N images (product 1B) are used for pixel-tracking. NASA's Automatic Registration and Orthorectification Package (AROP; Gao et al., 2009) is used to co-register ASTER images and DEMs to

3506

$\frac{dh}{dt}$ begins to “flatten” (see Rolstad et al., 2009 and Willis et al., 2012a for details on the method), which we estimate to be 1260 m by 1260 m (Fig. 9).

$\frac{dV}{dt}$ is multiplied by the density of glacier ice, set to 900 kg m^{-3} (e.g., Cuffey and Paterson, 2010) to produce an estimate of the mass change rate. Future ground-based measurements of densities on the CDI will be needed to find more accurate and precise values.

We have a sufficient number of ASTER DEMs to provide $\frac{dh}{dt}$ rates for 96 % of the total area of the icefield. Each pixel in the remaining small gaps is filled with the median $\frac{dh}{dt}$ value within 1 km. This is more accurate than using an elevation binning method or simply extrapolating an average rate. For example, the average low-elevation $\frac{dh}{dt}$ and overall average $\frac{dh}{dt}$ are both negative, these rates would not be suitable for filling a gap near the front of Garibaldi Glacier, which is known to be advancing and where we measure positive $\frac{dh}{dt}$ at low elevations.

We cannot directly measure changes in the sub-aqueous volume of ice, so we examine imagery of several glaciers that we know have advanced or retreated during the period covered by our study and use these to determine area change over water at the fronts of these glaciers. Once the area change is measured from available imagery, we assume an average depth below water of 150 m for Marinelli Glacier (see Koppes et al., 2009, Fig. 4a and b) and 60 m for the other glaciers, with an uncertainty of ± 50 m (the uncertainty on the change in area of each glacier is negligible). Dividing the sub-aqueous volume change by the time interval separating the images used to find area change gives the volume change rate. We add sub-aqueous volume change together for the glaciers we examine and combine that number with the overall mass loss rate derived from our $\frac{dh}{dt}$. This calculation is intended to show that sub-aqueous mass loss, while not well constrained in this study, is an order of magnitude lower than the overall mass change rate calculated from $\frac{dh}{dt}$.

Penetration of C-band radar into ice and (particularly) snow (e.g., Rignot et al., 2001) is a potential problem when using the SRTM DEM to estimate $\frac{dh}{dt}$. Willis et al. (2012b) compare X-band SRTM elevations (which should have negligible penetration)

3509

with C-band SRTM elevations and find approximately 2 m of C-band penetration over the SPI at all elevations. Due to a lack of X-band SRTM coverage over the CDI a similar analysis fails to provide any insight here, however, we perform our processing with 2 m added to every SRTM elevation, which increases our mass loss rate by about 13 %.

The CDI is colder than the SPI, which could lead to less wet conditions and greater penetration (Rignot et al., 2001), however, as noted above, we do not have adequate X-band data to quantify the difference. This effect should be considered when discussing mass loss from the CDI until such time as future studies help resolve the issue of radar penetration into ice and snow, which varies considerably depending on local conditions (Gardelle et al., 2012).

2.3 Velocities

In this section we describe how we use data from three different satellites with different resolutions to measure sub-pixel offsets and convert them to glacier velocities.

2.3.1 ASTER

Sub-pixel offsets between ASTER image pairs (pixel resolution of 15 m/pixel) are measured via normalized amplitude cross-correlation, with a spatial resolution of 120 m (i.e., a step size between cross-correlations of 8 pixels, see Melkonian, 2011 and Willis et al., 2012a for details). This technique, known as “pixel-tracking”, has been used to track velocities on many glaciers (e.g., Scambos et al., 1992; Stearns and Hamilton, 2005; Howat et al., 2008a; Willis et al., 2012a).

AROP is used to co-register the more recent scene in a pair of orthorectified ASTER images to the earlier scene to minimize misfits. The open source ROI_PAC’s “ampcor” routine (Rosen et al., 2004) is used to calculate E–W and N–S offsets. The results are post-filtered by excluding offsets with a signal-to-noise ratio (SNR, which is the peak cross-correlation value divided by the average) below a manually-selected threshold (Melkonian, 2011). A linear elevation-dependent correction (determined from apparent

3510

of $3.9 \pm 0.3 \text{ Gt yr}^{-1}$. Most mass loss (76 %) occurs in the ablation zone (which covers 60 % of the icefield area). Significant thinning at Marinelli Glacier, Darwin Glacier, and CDI-08 Glacier accounts for $1.4 \pm 0.1 \text{ km}^3 \text{ yr}^{-1}$ (31 %) of the icefield's volume loss.

Some thickening is occurring on the southern and south-facing areas of the icefield. This is most apparent at Garibaldi Glacier, where there are extensive positive $\frac{dh}{dt}$ throughout the ablation zone. This is consistent with Garibaldi's advance of $\sim 1 \text{ km}$ between 2003 and 2011 (Fig. 7). Table 1 gives the $\frac{dV}{dt}$ for the 16 largest glaciers, with rates for the entire basin, the accumulation zone and the ablation zone.

3.2 Velocities

Pixel-tracking is successfully applied to twenty ASTER image pairs, one QB02 pair and two ALOS pairs with acquisition dates between August 2001 and August 2011 (Fig. 8). ASTER pixel-tracking generally performs better on the northern half of the CDI as there is less cloud cover than to the south (Holmlund and Fuenzalida, 1995; Strelin and Iturraspe, 2007). Composite speed results are shown in Fig. 2, velocities for individual pairs over selected glaciers are shown in Fig. 3.

Average front speeds for the tidewater Marinelli Glacier 133 km^2 – the largest glacier of the CDI, (e.g., Koppes et al., 2009) are obtained between 09/07/2001 and 09/25/2001 (18 days) and 09/06/2003–09/13/2003 (7 days) from optical image pairs acquired by ASTER. In order to capture recent rapid motions at the front, we process a 07/16/2011 to 08/30/2011 QB02 pair (Fig. 4).

The Marinelli Glacier retreated $\sim 4 \text{ km}$ between 2001 and 2011 (measured from ASTER and QB02 imagery). Speed at the front reaches a maximum of $\sim 7.5 \pm 0.2 \text{ m day}^{-1}$ in 2001, accelerating to $\sim 9.5 \pm 0.6 \text{ m day}^{-1}$ in 2003 and a peak of $\sim 10 \pm 0.3 \text{ m day}^{-1}$ in 2011. Fig. 4 shows a map of the 2011 velocities from the QB02 pair, along with longitudinal speed profiles for several pairs that highlight the high front speed and acceleration of about 30 % from 2001 to 2011.

3513

Speeds at the front of the tidewater Darwin Glacier (46 km^2), one of three major contributors to thinning, reach a maximum average of $9.7 \pm 0.8 \text{ m day}^{-1}$ for the period 09/25/2001 to 10/02/2001. No repeat measurements of motion from ASTER pairs are available for the Darwin Glacier. CDI-08 (127 km^2), the furthest west and south of the three most rapidly-thinning glaciers, reaches speeds of $2.0 \pm 0.5 \text{ m day}^{-1}$ within 1 km of its 01/15/2011 front (01/04/2011 to 02/19/2011 ALOS pair), unfortunately repeat speeds are not available for this glacier.

4 Discussion

4.1 Elevation Change Rates

4.1.1 Impact of ELA

Given the considerable uncertainty and variability of the regional ELA, we investigate the impact of changing the regional ELA on the $\frac{dV}{dt}$ for the whole icefield. An ELA of about 650 m has been found at the glaciers on the western and southern sides of the CDI (Bown et al., 2013), we perform processing using this as the regional ELA instead of 1090 m. The lower ELA produces a mass loss rate of $3.4 \pm 0.2 \text{ Gt yr}^{-1}$, which is only 10 % less than the mass loss rate (not including sub-aqueous mass change) with the higher ELA, as mass loss is concentrated at low elevations. Examining the impact of lowering the ELA highlights this concentration, as the percentage area of the ablation zone drops to 26 % yet it still accounts for 51 % of the mass loss.

4.1.2 Impact of allowed deviation from first elevation

The deviation allowed from the first elevation has a much larger impact on the mass loss rate. Changing the positive deviation allowed from +5 to +10 m yr^{-1} decreases the

3514

phase (e.g., Post et al., 2011). Jorge Montt Glacier on the SPI is a somewhat analogous TWG on the SPI, with a grounded front, thinning occurring at approximately the same rate, and a rapidly receding terminus (Rivera et al., 2012; Willis et al., 2012b). Front recession has opened fjords at both Marinelli and Jorge Montt, and rapid retreat was initiated as each glacier receded into deeper water (Holmlund and Fuenzalida, 1995; Koppes et al., 2009; Rivera et al., 2012). At Marinelli the retreat is thought to have been initiated by thinning linked to climate changes (Koppes et al., 2009). The fact that 2011 speeds at Marinelli are as high or higher than 2001 and 2003 suggests that the glacier has not yet retreated to fjord depths shallow enough to slow it down, and would lead us to expect further retreat until shallower depths are reached. Though there is significant variability from glacier to glacier on the Patagonian icefields (Rivera et al., 2012) the similar behavior of these two glaciers in the same region but on different icefields suggests that changing climate plays a role in retreat and thinning at Jorge Montt as well, given that the retreat was inferred to have been triggered by warming-induced thinning at the fronts of both glaciers.

Seasonal changes in conditions at Marinelli Glacier could be influencing our results, we note that the two ASTER pairs from which we obtain front speeds are both from September. However, it is possible that the speeds in September 2001 and 2003 are different due to inter-annual variations in the onset of conditions affecting the glacier.

The 2011 QuickBird 2 pair is from 07/30/2011 to 08/16/2011. While this is not an entirely different season from the ASTER pairs, it is a month earlier, which is long enough for seasonal variations to possibly play a role in any observed speed differences. We consider it unlikely, however, that a seasonal component of motion is dominant in the 30 % increase in the front speed at Marinelli between September 2001 (7.5 m day^{-1}) and August 2011 (10 m day^{-1}). Unfortunately, we do not have enough repeat measurements to quantify any seasonal effect on speeds, especially given that our ALOS results over Marinelli from the austral summer do not reach the front.

3519

4.2.2 Other CDI Glaciers

Based on the $\frac{dh}{dt}$ results for Darwin Glacier, which have the same general pattern of thinning, we predict sustained, high front speeds similar to those observed at Marinelli Glacier. ALOS velocities show CDI-08 also speeds up towards its front (typical of tide-water glaciers) and is slower than either the Marinelli or Darwin Glacier, but there are no earlier speeds available to see what impact thinning there has had. Many of the non-tidewater terminating CDI glaciers slow down towards their fronts (e.g. Roncagli, Fig. 3c). The different thicknesses, bedrock topography and surface slopes of the glaciers on the CDI contribute to the variety of dynamic regimes observed.

5 Conclusions

Rapid thinning at three outlet glaciers on the CDI: Marinelli Glacier, Darwin Glacier, and CDI-08 Glacier, accounts for 31 % of the total volume loss rate (~ 1.4 out of $4.3 \text{ km}^3 \text{ yr}^{-1}$). Elevation profiles and optical imagery indicate that while Marinelli Glacier and Darwin Glacier have undergone significant retreat, they remain grounded at their fronts. Climate records from the 1940's through the 1990's show a warming trend in this region, which leads to higher temperatures along with decreased precipitation on the northern side of the icefield and an increase in precipitation on the southern side (Holmlund and Fuenzalida, 1995; Strelin and Iturraspe, 2007). Locally calibrated climate model results indicate a trend of warming and decreased snow input for Marinelli Glacier from the 1950's to 2009 (Koppes et al., 2009). These conditions have led to consistently negative mass balance on northern glaciers such as Marinelli throughout much of the 20th century, initiating thinning that caused the rapid retreat observed here and in several previous studies (Holmlund and Fuenzalida, 1995; Strelin and Iturraspe, 2007; Koppes et al., 2009). While the northern side is thinning, thickening is observed on individual southern and western glaciers, most notably Garibaldi Glacier, where measurements of positive $\frac{dh}{dt}$ are in keeping with its continued advance.

3520

Our limited repeat glacier speed measurements are consistent with our $\frac{dh}{dt}$ observations. The maximum front speed of Marinelli Glacier goes up by about 30% as the front retreats between 2001 and 2011, with most of our measured acceleration occurring between 2001 and 2003. We would expect to observe the same pattern of sustained or accelerating front speeds at Darwin and CDI-08 Glacier (due to the ongoing retreat at these glaciers), but lack the requisite repeat measurements.

As is the case for the NPI and SPI, the CDI is losing mass relatively rapidly. The NPI covers an area of approximately 4000 km² and has an average $\frac{dh}{dt}$ of -1.1 ± 0.1 m yr⁻¹ (Willis et al., 2012b), less than the CDI (-1.7 ± 0.1 m yr⁻¹). The SPI covers 12,596 km² (Casassa et al., 2013) and has an average $\frac{dh}{dt}$ of -1.8 ± 0.1 m yr⁻¹ (Willis et al., 2012b), very close the CDI rate. The average $\frac{dh}{dt}$ for CDI, however, is significantly more negative than the Juneau Icefield in Alaska (~4000 km²), which has an average $\frac{dh}{dt}$ of -0.09 ± 0.03 m yr⁻¹ (Melkonian, 2011).

Acknowledgements. ASTER data was provided by the LPDAAC. We thank the Alaska Satellite Facility (ASF) and the Japan Aerospace Exploration Agency (JAXA) for the ALOS data. Supported by NASA grant NNX08AI87G issued through the Science Mission Directorates Earth Science Division. Andrés Rivera and Francisca Bown acknowledge the GLIMS project for providing free satellite imagery in the full glacier inventory and surface variations coming in a separate book chapter. QuickBird 2 and WorldView 1 images provided by NGA Commercial Imagery Program. Sasha A. Bernstein was partially supported by the Cornell Rawlings Presidential Research Scholars Program.

3521

References

- Ahn, Y. and Howat, I. M.: Efficient Automated Glacier Surface Velocity Measurement From Repeat Images Using Multi-Image/Multichip and Null Exclusion Feature Tracking, 49, 2838–2846, 2011. 3511
- Arendt, A. A., Echelmeyer, K. A., Harrison, W. D., Lingle, C. S., and Valentine, V. B.: Rapid wastage of Alaska glaciers and their contribution to rising sea level., *Science (New York, N.Y.)*, 297, 382–6, doi:10.1126/science.1072497, 2002. 3505
- Aster, R. C., Borchers, B., and Thurber, C. H.: *Parameter Estimation and Inverse Problems*, Elsevier Inc., Burlington, MA, 2005. 3508
- Benn, D. I. and Evans, D. J.: *Glaciers & Glaciology*, Oxford University Press Inc., New York, 1998. 3516
- Berthier, E., Arnaud, Y., Kumar, R., Ahmad, S., Wagnon, P., and Chevallier, P.: Remote sensing estimates of glacier mass balances in the Himachal Pradesh (Western Himalaya, India), *Remote Sensing of Environment*, 108, 327–338, doi:10.1016/j.rse.2006.11.017, 2007. 3505
- Berthier, E., Schiefer, E., Clarke, G. K. C., Menounos, B., and Rémy, F.: Contribution of Alaskan glaciers to sea-level rise derived from satellite imagery, *Nat. Geosci.*, 3, 92–95, doi:10.1038/ngeo737, 2010. 3505, 3507
- Bown, F., Rivera, A., Zenteno, P., Bravo, C., and Cawkwell, F.: First glacier inventory and recent glacier variations of Isla Grande de Tierra del Fuego and adjacent islands in Southern Chile, in: *Global Land Ice Measurements from Space*, edited by: Kargel, J. S., Leonard, G. J., Bishop, M. P., Kääb, A., and Raup, B., Praxis-Springer (Publishers), Heidelberg, ISBN: 978-3-540-79817-0, 2013. 3505, 3514
- Casassa, G., Rodríguez, J. L., Rivera, A., and Bown, F.: A new glacier inventory for the Southern Patagonia Icefield and areal changes 1986–2000, in: *Global Land Ice Measurements from Space*, edited by: Kargel, J. S., Leonard, G. J., Bishop, M. P., Kääb, A., and Raup, B., Praxis-Springer (Publishers), Heidelberg, ISBN: 978-3-540-79817-0, 2013. 3521
- Cuffey, K. M. and Paterson, W. S. B.: *The Physics of Glaciers*, Butterworth-Heinemann, 4 Edn., 2010. 3509, 3518
- Fujisada, H., Bailey, G., Kelly, G., Hara, S., and Abrams, M.: ASTER DEM performance, *IEEE T. Geosci. Remote*, 43, 2707–2714, doi:10.1109/TGRS.2005.847924, 2005. 3506, 3507

3522

- Gao, F., Masek, J., and Wolfe, R. E.: Automated registration and orthorectification package for Landsat and Landsat-like data processing, *J. Appl. Remote Sens.*, 3, 033515, doi:10.1117/1.3104620, 2009. 3506
- Gardelle, J., Berthier, E., and Arnaud, Y.: Impact of resolution and radar penetration on glacier elevation changes computed from DEM differencing, *J. Glaciol.*, 58, 419–422, doi:10.3189/2012JoG11J175, 2012. 3510
- 5 Glasser, N. F., Harrison, S., Jansson, K. N., Anderson, K., and Cowley, A.: Global sea-level contribution from the Patagonian Icefields since the Little Ice Age maximum, *Nat. Geosci.*, 1–5, doi:10.1038/ngeo1122, 2011. 3505
- 10 Holmlund, P. and Fuenzalida, H.: Anomalous glacier responses to 20th century climatic changes in Darwin Cordillera, southern Chile, *J. Glaciol.*, 41, 465–473, 1995. 3505, 3508, 3513, 3515, 3517, 3519, 3520
- Howat, I. M., Joughin, I., Fahnestock, M., Smith, B. E., and Scambos, T. A.: Synchronous retreat and acceleration of southeast Greenland outlet glaciers 2000–06: ice dynamics and coupling to climate, *J. Glaciol.*, 54, 646–660, doi:10.3189/002214308786570908, 2008a. 3510
- 15 Howat, I. M., Smith, B. E., Joughin, I., and Scambos, T. A.: Rates of southeast Greenland ice volume loss from combined ICESat and ASTER observations, *Geophys. Res. Lett.*, 35, 1–5, doi:10.1029/2008GL034496, 2008b. 3507, 3508
- Koppes, M., Hallet, B., and Anderson, J.: Synchronous acceleration of ice loss and glacial erosion, *Glaciar Marinelli, Chilean Tierra del Fuego, J. Glaciol.*, 55, 207–220, doi:10.3189/002214309788608796, 2009. 3504, 3505, 3509, 3513, 3515, 3516, 3518, 3519, 3520
- 20 Koppes, M., Conway, H., Rasmussen, L. A., and Chernos, M.: Deriving mass balance and calving variations from reanalysis data and sparse observations, *Glaciar San Rafael, northern Patagonia, 1950–2005, The Cryosphere*, 5, 791–808, doi:10.5194/tc-5-791-2011, 2011. 3508
- 25 Lopez, P., Chevallier, P., Favier, V., Pouyaud, B., Ordenes, F., and Oerlemans, J.: A regional view of fluctuations in glacier length in southern South America, *Glob. Planet. Change*, 71, 85–108, doi:10.1016/j.gloplacha.2009.12.009, 2010. 3505, 3506, 3515
- 30 Masiokas, M. H., Rivera, A., Espizua, L. E., Villalba, R., Delgado, S., and Aravena, J. C.: Glacier fluctuations in extratropical South America during the past 1000 years, *Palaeogeogr. Palaeoclim.*, 281, 242–268, doi:10.1016/j.palaeo.2009.08.006, 2009. 3505, 3517

3523

- Melkonian, A. K.: Measuring Glacier Velocities and Elevation Change Rates from ASTER Data for the Juneau Icefield, Alaska, M.s. thesis, Cornell University, 2011. 3507, 3510, 3521
- Nuth, C. and Kääb, A.: Co-registration and bias corrections of satellite elevation data sets for quantifying glacier thickness change, *The Cryosphere*, 5, 271–290, doi:10.5194/tc-5-271-2011, 2011. 3511
- 5 Post, A., O’Neel, S., Motyka, R. J., and Streveler, G.: A Complex Relationship Between Calving Glaciers and Climate, *EOS Transactions, Am. Geophys. Union*, 92, 2011. 3519
- Pritchard, H. D. and Vaughan, D. G.: Widespread acceleration of tidewater glaciers on the Antarctic Peninsula, *J. Geophys. Res.*, 112, 1–10, doi:10.1029/2006JF000597, 2007. 3506
- 10 Quintana, J.: Estudio de los factores que explican la variabilidad de la precipitación en Chile en escalas de tiempo interdecadal, Msc thesis, Universidad de Chile, 2004. 3505
- Rasmussen, L. A., Conway, H., and Raymond, C. F.: Influence of upper air conditions on the Patagonia Icefields, *Glob. Planet. Change*, 59, 203–216, doi:10.1016/j.gloplacha.2006.11.025, 2007. 3508
- 15 Rignot, E., Echelmeyer, K., and Krabill, W.: Penetration depth of interferometric synthetic-aperture radar signals in snow and ice, *Geophys. Res. Lett.*, 28, 3501–3504, doi:10.1029/2000GL012484, 2001. 3509, 3510
- Rignot, E., Rivera, A., and Casassa, G.: Contribution of the Patagonia Icefields of South America to sea level rise., *Science (New York, N.Y.)*, 302, 434–7, doi:10.1126/science.1087393, 2003. 3505, 3508
- 20 Rivera, A., Benham, T., Casassa, G., Bamber, J., and Dowdeswell, J.: Ice elevation and areal changes of glaciers from the Northern Patagonia Icefield, Chile, *Glob. Planet. Change*, 59, 126–137, doi:10.1016/j.gloplacha.2006.11.037, 2007. 3505, 3507
- Rivera, A., Koppes, M., Bravo, C., and Aravena, J. C.: Little Ice Age advance and retreat of Glaciar Jorge Montt, Chilean Patagonia, *Climate of the Past*, 8, 1–12, doi:10.5194/cp-8-1-2012, 2012. 3519
- 25 Rolstad, C., Haug, T., and Denby, B.: Spatially integrated geodetic glacier mass balance and its uncertainty based on geostatistical analysis: application to the western Svartisen ice cap, Norway, *J. Glaciol.*, 55, 666–680, doi:10.3189/002214309789470950, 2009. 3508, 3509
- 30 Rosen, P. A., Henley, S., Peltzer, G., and Simons, M.: Updated Repeat Orbit Interferometry Package, *EOS, Trans. Am. Geophys. Union*, 85, 47, doi:10.1029/2004EO050004, 2004. 3510

3524

- San, B. T. and Süzen, M. L.: Digital elevation model (DEM) generation and accuracy assessment from ASTER stereo data, *Int. J. Remote Sens.*, 26, 5013–5027, doi:10.1080/01431160500177620, 2005. 3507
- Scambos, T. A., Dutkiewicz, M. J., Wilson, J. C., and Bindschadler, R. A.: Application of Image Cross-Correlation to the Measurement of Glacier Velocity Using Satellite Image Data, *Remote Sens. Environ.*, 42, 177–186, 1992. 3510
- Stearns, L. and Hamilton, G.: A new velocity map for Byrd Glacier, East Antarctica, from sequential ASTER satellite imagery, *Ann. Glaciol.*, 41, 71–76, doi:10.3189/172756405781813393, 2005. 3510
- 10 Strelin, J. and Iturraspe, R.: Recent evolution and mass balance of Cordón Martial glaciers, Cordillera Fueguina Oriental, *Glob. Planet. Change*, 59, 17–26, doi:10.1016/j.gloplacha.2006.11.019, 2007. 3505, 3508, 3513, 3517, 3520
- Strelin, J., Casassa, G., Rosqvist, G., and Holmlund, P.: Holocene glaciations in the Ema Glacier valley, Monte Sarmiento Massif, Tierra del Fuego, *Palaeogeogr. Palaeoclim.*, 260, 299–314, doi:10.1016/j.palaeo.2007.12.002, 2008. 3504
- 15 Tucker, C. J., Grant, D. M., and Dykstra, J. D.: NASAs Global Orthorectified Landsat Data Set, *Photogr. Eng. Rem. Sens.*, 70, 313–322, 2004. 3507
- Warren, C. R. and Aniya, M.: The calving glaciers of southern South America, *Glob. Planet. Change*, 22, 59–77, 1999. 3518
- 20 Willis, M. J., Melkonian, A. K., Pritchard, M. E., and Ramage, J. M.: Ice Loss Rates at the Northern Patagonian Icefield Derived Using a Decade of Satellite Remote Sensing, *Remote Sens. Environ.*, doi:10.1016/j.rse.2011.09.017, 2012a. 3505, 3506, 3507, 3509, 3510, 3511
- Willis, M. J., Melkonian, A. K., Pritchard, M. E., and Rivera, A.: Ice Loss from the Southern Patagonian Icefield, South America, between 2000 and 2012, *Geophys. Res. Lett.*, 2012b. 3505, 3509, 3519, 3521
- 25

3525

Table 1. Volume Change Rates for the 16 Largest Outlet Glaciers on the CDI (includes estimates of sub-aqueous volume change for Marinelli, CDI-08, Garibaldi and Darwin).

Glacier	Area (km ²)	$\frac{dV}{dt}$ (km ³ yr ⁻¹)	Uncertainty (km ³ yr ⁻¹)	Ablation Area (km ²)	$\frac{dV}{dt}$ (km ³ yr ⁻¹)	Uncertainty (km ³ yr ⁻¹)	Accumulation Area (km ²)	$\frac{dV}{dt}$ (km ³ yr ⁻¹)	Uncertainty (km ³ yr ⁻¹)
Marinelli Glacier	132.93	-0.74	0.08	81.45	-0.68	0.07	51.48	-0.06	0.03
CDI-08 Glacier	127.42	-0.43	0.05	36.45	-0.26	0.03	90.97	-0.16	0.04
Roncagli Glacier	116.06	-0.18	0.07	42.23	-0.12	0.04	73.83	-0.06	0.05
Stoppani Glacier	102.04	-0.2	0.05	39.02	-0.12	0.04	63.03	-0.08	0.03
Garibaldi Glacier	63.86	0.02	0.07	21.01	0.04	0.05	42.85	-0.03	0.05
CDI.157 Glacier	57.42	-0.11	0.04	49.9	-0.09	0.03	7.52	-0.02	0.02
de.la.Vedova Glacier	56.83	-0.15	0.03	21.59	-0.07	0.02	35.24	-0.08	0.03
Bahia_Broken Glacier	53.22	-0.1	0.04	12.12	-0.04	0.02	41.1	-0.07	0.03
CDI.150 Glacier	52.31	-0.02	0.03	18.1	-0.0	0.02	34.21	-0.01	0.03
CDI.456 Glacier	51.22	-0.03	0.04	19.84	-0.02	0.02	31.39	-0.0	0.04
Darwin Glacier	45.61	-0.18	0.03	16.99	-0.14	0.02	28.62	-0.05	0.02
Cuevas Glacier	45.27	-0.06	0.04	4.58	-0.01	0.01	40.69	-0.05	0.04
CDI.455 Glacier	37.73	0.02	0.04	7.53	0.01	0.01	30.2	0.01	0.04
Oblicuo Glacier	29.81	0.02	0.05	19.38	0.01	0.04	10.43	0.01	0.02
CDI.48 Glacier	28.58	-0.04	0.02	20.68	-0.03	0.02	7.9	-0.01	0.01
CDI.142 Glacier	26.79	-0.05	0.04	12.55	-0.02	0.02	14.24	-0.03	0.03

3526

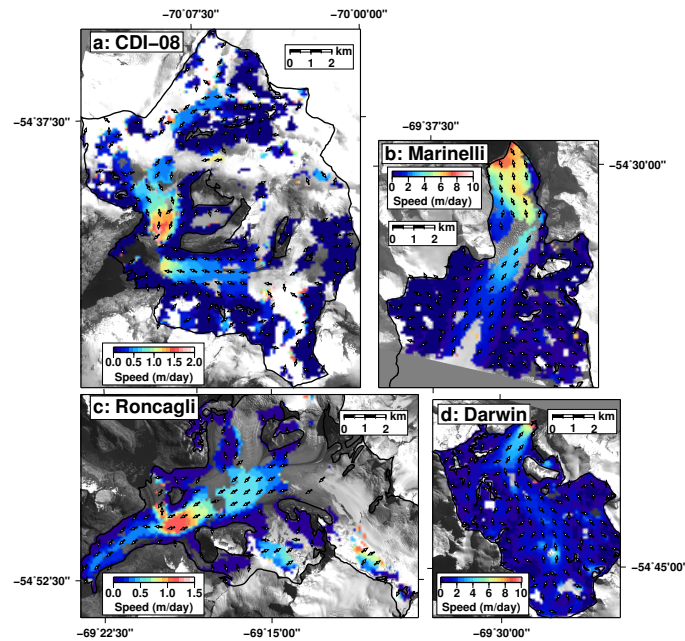


Fig. 3. Velocity maps for individual glaciers (separate color scale for each map), highlighting the quality of the velocity results for individual image pairs. **(a)** shows velocities from the 01/04/2011–02/19/2011 ALOS pair for CDI-08 Glacier with an ASTER image from 01/15/2011 in the background. **(b)** shows velocities from the 08/07/2001–09/25/2001 ASTER pair for Marinelli Glacier with an ASTER image from 09/07/2001 in the background. **(c)** shows velocities from the 01/04/2011–02/19/2011 ALOS pair for Roncagli Glacier with an ASTER image from 02/07/2002 in the background. **(d)** shows velocities from the 09/25/2001–10/02/2001 ASTER pair for Darwin Glacier with an ASTER image from 09/25/2001 in the background.

3529

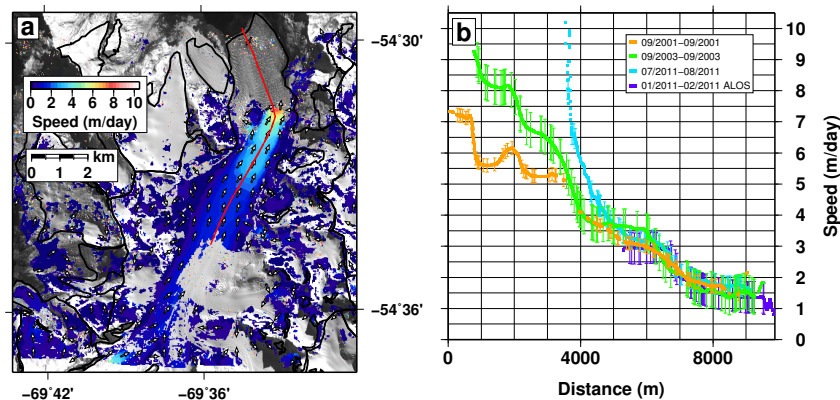


Fig. 4. Speeds for Marinelli Glacier. Panel **(a)** is a map of velocities from the QB02 (07/30/2011–08/16/2011) pair (background is the 09/07/2001 ASTER V3N image). Panel **(b)** shows profiles (indicated by the red line in panel **(a)**) from two ASTER pairs (09/07/2001–09/25/2001, 09/06/2003–09/13/2003), the QB02 pair and an ALOS pair (01/04/2011–02/19/2011). The QB02 velocities extend to the 2011 front, comparing them with the 2001 ASTER V3N image and the ASTER speed profiles highlights the ~ 4 km of front retreat between 2001 and 2011. Marinelli Glacier accelerates at its front from a maximum of $7.5 \pm 0.2 \text{ m day}^{-1}$ in 2001, to $9.5 \pm 0.6 \text{ m day}^{-1}$ in 2003 to a peak of $\sim 10 \pm 0.3 \text{ m day}^{-1}$ in 2011. While the maximum speed from 2003 to 2011 does not change significantly, the speed profiles show a clear acceleration between 2003 to 2011 from the 2011 front to a distance of 5000 m on the profile.

3530

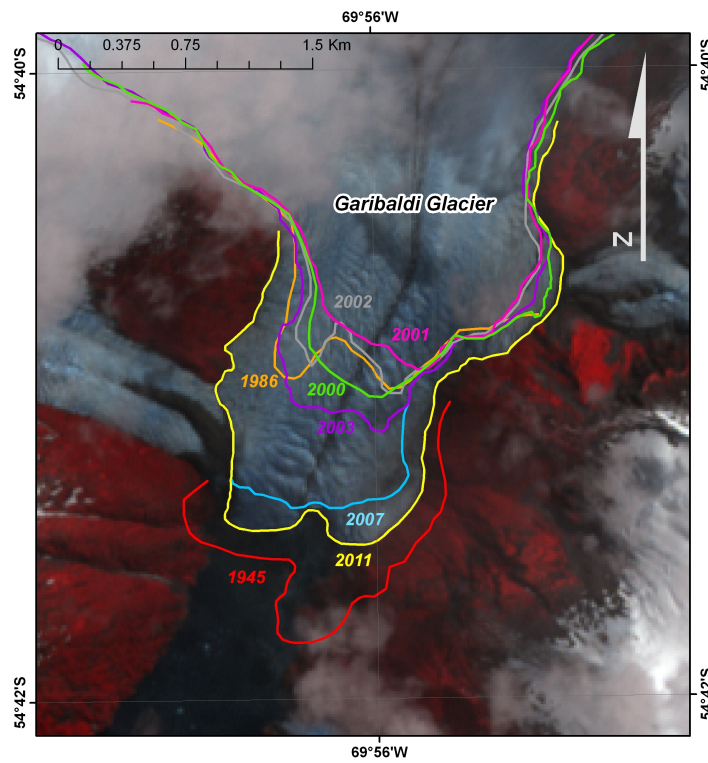


Fig. 7. Frontal variation history of Garibaldi Glacier from Landsat TM, ASTER and aerial photographs. The background is a 01/15/2011 ASTER image.

3533

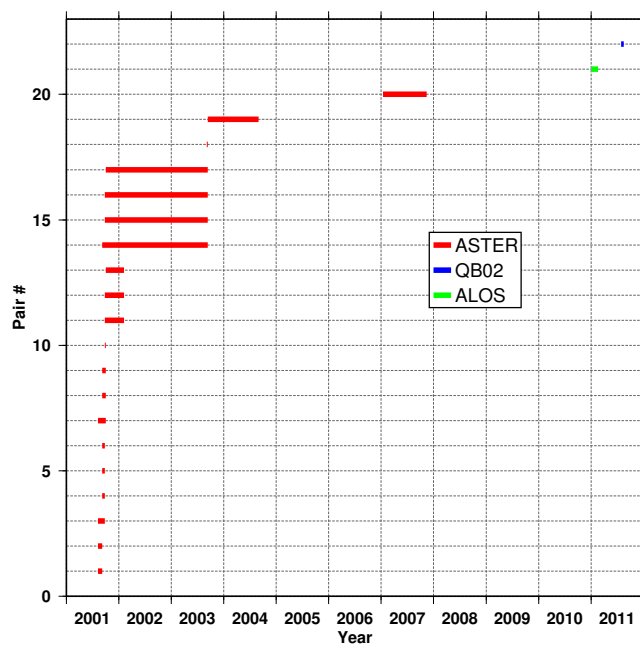


Fig. 8. Date intervals for 22 pairs that produce usable pixel-tracking results. The most recent is a QB02 pair (blue), the next most recent is an ALOS pair (green), and the remainder are ASTER pairs (red). These are from a total of 1 QB02 pair, 3 ALOS pairs and 119 ASTER pairs processed.

3534

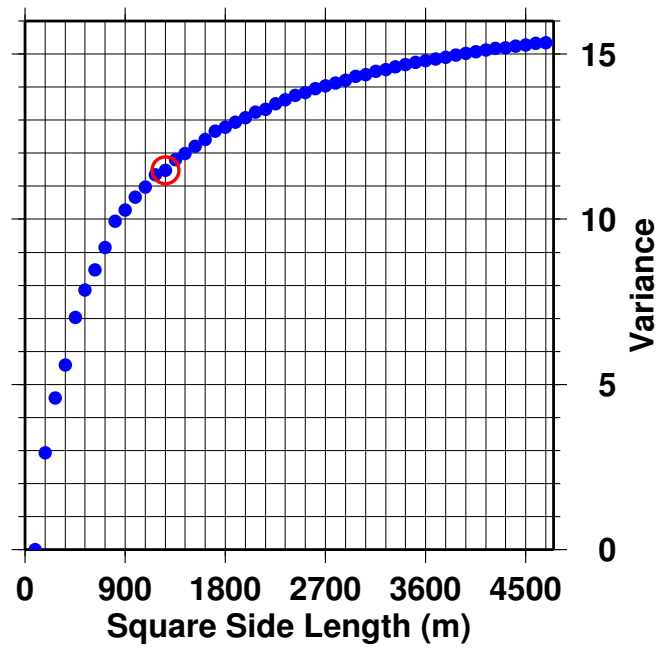


Fig. 9. A plot of pixel size (listed as side length of square pixel) vs. variance of bedrock $\frac{dh}{dt}$, plotted as blue dots. Red circle indicates selected “corner” point, 1260 m is selected as the area of maximum correlation for the $\frac{dh}{dt}$ variance.

3535

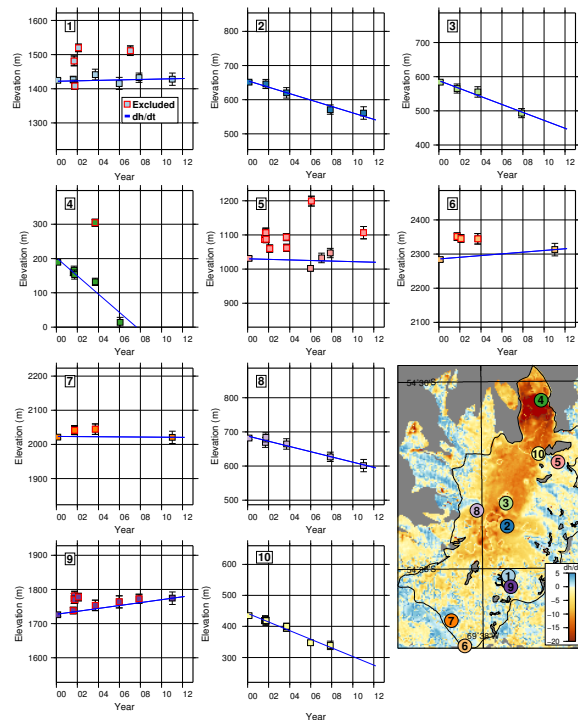


Fig. 10. Elevation values and $\frac{dh}{dt}$ for randomly selected pixels over Marinelli Glacier. The left-most elevation in each graph is the SRTM elevation at that pixel. Blue lines indicate the $\frac{dh}{dt}$ calculated for each pixel, elevation points bolded red are excluded from $\frac{dh}{dt}$ calculation. The bottom right panel shows the $\frac{dh}{dt}$ map, with numbered circles indicating the location corresponding to each graph.

3536

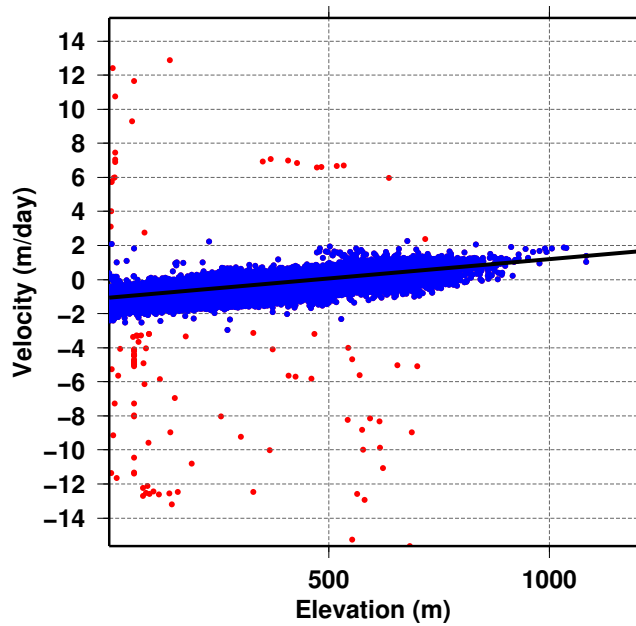


Fig. 11. Scatter plot of E–W “bedrock” velocities for the 09/07/2001 to 09/25/2001 ASTER pair. The black line shows the linear trend fitted to the blue points, this is removed from the overall E–W velocity results. Red points are excluded when fitting the trend (they are greater than $\pm\sigma$ from the median value). This cutoff makes a negligible difference in the trend for this pair, but for other pairs it can change the trend significantly (e.g. $>1 \text{ m day}^{-1}$ per 1000 m elevation).

3537

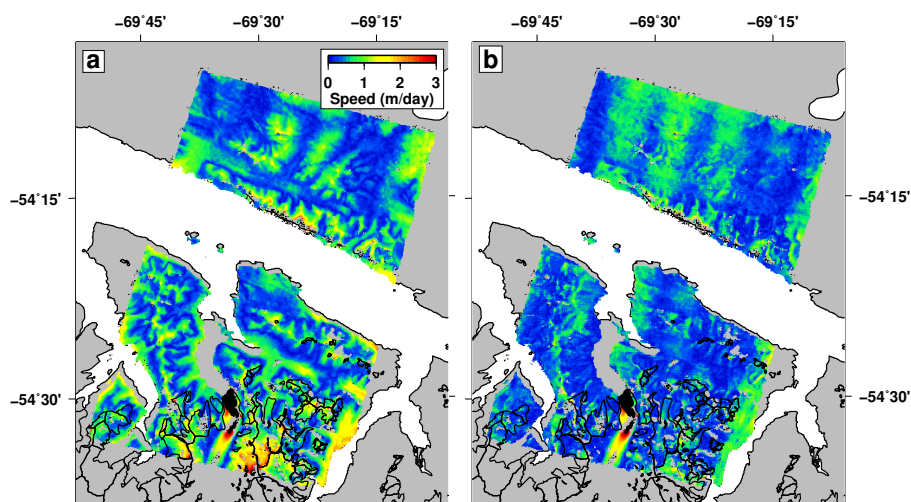


Fig. 12. Effect of elevation-dependent velocity correction for 09/07/2001 to 09/25/2001 ASTER image pair covering Marinelli Glacier. Glacier outlines in black, bedrock in gray (correction is not applied to water pixels). Panel (a) is a map of speeds with no correction applied, panel (b) is a map of speeds with correction applied. Correction significantly reduces bedrock motion, the mean and standard deviation for the entire pair drops from 0.6 ± 0.4 for the uncorrected speeds to 0.4 ± 0.3 for the corrected speeds.

3538